

Active Learning in Brain Tumor Segmentation with Uncertainty Sampling, Annotation Redundancy Restriction, and Data Initialization

Running Title: Active Learning in Brain Tumor Imaging

Daniel D Kim^{1,2,†}, Rajat S Chandra^{3,†}, Jian Peng^{4,†}, Jing Wu⁴, Xue Feng⁵, Michael Atalay^{1,2}, Chetan Bettegowda⁶, Craig Jones^{6,7}, Haris Sair⁶, Wei-hua Liao⁴, Chengzhang Zhu⁸, Beiji Zou⁹, Li Yang⁴, Anahita Fathi Kazerooni^{10,11}, Ali Nabavizadeh^{10,12}, Harrison X Bai⁶, and Zhicheng Jiao^{1,2}

¹ Warren Alpert Medical School of Brown University, Providence RI, USA

² Department of Diagnostic Imaging, Rhode Island Hospital, Providence, RI, USA

³ Perelman School of Medicine at the University of Pennsylvania, Philadelphia, PA, USA

⁴ Second Xiangya Hospital of Central South University, Changsha, Hunan, China

⁵ Biomedical Engineering, University of Virginia, Charlottesville, VA, USA

⁶ Department of Radiology, Johns Hopkins University, Baltimore, MD, US

⁷ Department of Computer Science, Johns Hopkins University, Baltimore, MD, US

⁸ College of Literature and Journalism, Central South University, Changsha, China

⁹ School of Computer Science and Engineering, Central South University, Changsha, China

¹⁰ Center for Data-Driven Discovery in Biomedicine (D³b), Children's Hospital of Philadelphia, Philadelphia, PA, USA

¹¹ Department of Neurosurgery, Perelman School of Medicine, University of Pennsylvania, Philadelphia, PA, USA

¹² Department of Radiology, Perelman School of Medicine, University of Pennsylvania, Philadelphia, PA, USA

†DDK, RSC, and JP contributed equally to this work and share co-first authorship

Corresponding Author:

Zhicheng Jiao, Department of Radiology, Brown University

593 Eddy St, Rhode Island Hospital, Department of Diagnostic Imaging, Providence, RI, 02903,
USA

zhicheng_jiao@brown.edu

ABSTRACT

Deep learning models have demonstrated great potential in medical imaging, but their development is limited by the expensive, large volume of annotated data required. Active learning (AL) addresses this by training a model on a subset of the most informative data samples without compromising performance. We compared different AL strategies and propose a framework that minimizes the amount of data needed for state-of-the-art performance. 638 multi-institutional brain tumor MRI images were used to train a 3D U-net model and compare AL strategies. We investigated uncertainty sampling, annotation redundancy restriction, and initial dataset selection techniques. Uncertainty estimation techniques including Bayesian estimation with dropout, bootstrapping, and margins sampling were compared to random query. Strategies to avoid annotation redundancy by removing similar images within the to-be-annotated subset were considered as well. We determined the minimum amount of data necessary to achieve similar performance to the model trained on the full dataset ($\alpha = 0.1$). A variance-based selection strategy using radiomics to identify the initial training dataset is also proposed. Bayesian approximation with dropout at training and testing showed similar results to that of the full data model with less than 20% of the training data ($p=0.293$) compared to random query achieving similar performance at 56.5% of the training data ($p=0.814$). Annotation redundancy restriction techniques achieved state-of-the-art performance at approximately 40%-50% of the training data. Radiomics dataset initialization had higher Dice with initial dataset sizes of 20 and 80 images, but improvements were not significant. In conclusion, we investigated various AL strategies with dropout uncertainty estimation achieving state-of-the-art performance with the least annotated data.

1 INTRODUCTION

Deep learning in medical imaging has made significant progress, achieving near or superior performance to that of human expert annotators.¹ Despite the strides in performance, these models are limited by requiring substantial training data and annotations, which are expensive and time-consuming to produce.²

Active learning (AL) is a strategy that identifies a subset of unannotated data that would be most informative so that a model can be trained on a subset of annotated samples without compromising performance. Models are built iteratively until acceptable performance is achieved.

AL strategies generally have two approaches: (a) calculating uncertainty and annotating the most uncertain or difficult images or (b) grouping images based on similarity and selecting a subset from each similarity group to identify a representative cohort.² To identify uncertain images, Wang et. al uses a preliminary model to predict on unannotated data and assigns images with the smallest probability of the most probable class as most uncertain.³ An ensemble approach that identifies images with the most disagreement among models can also be used.⁴ Bayesian neural networks have alternatively been proposed to use one model to generate a probability distribution instead of a single probability, and wider distributions are attributed to higher uncertainty.^{5,6} To reduce annotation redundancy, Yang et. al compares the output from convolutional neural networks, which are ultimately high-level feature vectors, to assess the similarity of unannotated images and identify a representative set of images to annotate.³ Similarly, traditional computer vision techniques have also been used for feature extraction.⁷ Kim et. al combines both uncertainty and representativeness techniques when selecting data to annotate for skin lesion classification and segmentation.⁸

Many AL strategies, including the ones above, focus on 2D imaging, classification tasks, or non-medical imaging.^{2-4,6,7} However, application of validated techniques onto 3D medical imaging, such as magnetic resonance imaging (MRI) or computerized tomography (CT), is not straightforward. Some medical imaging tasks have an additional complexity in that they focus on a small region of interest (ROI). Prognosis of brain cancer for example focuses on contrast-enhancing tumor, which is much smaller than the whole brain.⁹ This characteristic is exacerbated in 3D imaging as uncertainty calculations need to focus on a small portion of voxels of interest, making them sensitive to noise from the substantial background. Sharma et. al demonstrates remarkable success here by combining least confidence uncertainty estimation and

representativeness to create a high performing model using less than 15% of the 2018 Brain Tumor Segmentation (BraTS) dataset.¹⁰ Other works have pursued active learning in 3D medical imaging by incorporating reinforcement learning rather than traditional uncertainty and representative strategies.^{11,12}

In this paper, we contribute further to AL in 3D medical imaging with a pilot study by comparing multiple uncertainty and representative techniques and evaluating their individual contribution in reducing the annotation burden on real-world, multi-institutional clinical brain tumor MRI data.

2 MATERIALS AND METHODS

2.1 Neural Network Architecture

A 5-layered 3D U-net neural network architecture was used.¹³ Models used both contrast-enhanced T1-weighted (T1ce) and T2-weighted (T2) sequences to segment the contrast enhancing region. Two patches of size $128 \times 128 \times 128$ biased 25% to the ROI from each image were used for model training. Data augmentation included scaling, rotation, and flipping transformations. Models optimized a soft Dice loss function on the validation set until there was no improvement for 50 epochs. During validation and testing, the full image was inputted. All models were trained using a 16 GB NVIDIA V100 Tensor Core graphical processing unit (GPU). Detailed hyperparameter settings are available in the published study on the full data model.¹⁴

2.2 Active Learning Algorithm

Our proposed methods to improve AL for 3D image segmentation consists of three major components: (1) uncertainty sampling, (2) annotation redundancy restriction, and (3) initial dataset selection (Figure 1).

Uncertainty sampling first uses a model trained on a smaller subset of data to predict segmentations on unannotated data. Uncertainty is calculated from the predicted segmentations, and k images with the highest uncertainty are chosen for annotation. Uncertainty scores estimate the model's confidence on data that was not included in training. Three different uncertainty estimating techniques are outlined below.

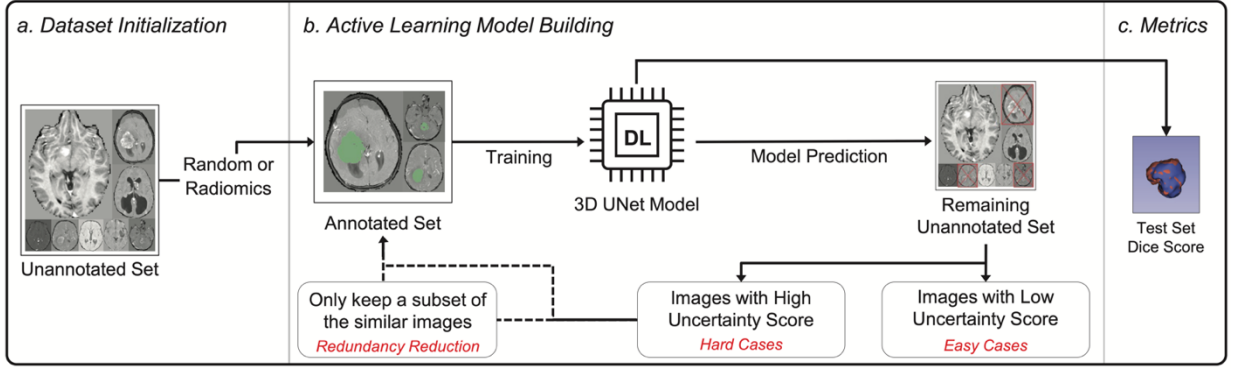


Figure 1. Workflow of the full active learning framework

The first technique involves bootstrapping. At each AL iteration, n bootstrapped datasets are generated by sampling with replacement and used to train a separate model. Higher variance in predictions across models suggests ensemble disagreement and higher uncertainty.⁴ The uncertainty score is the mean of the variance map of all of the probability maps returned from each bootstrapped model.

Next, we discuss margins sampling. One model is trained on the current batch of annotated data. Each voxel-probability within a probability map p_i for image i can range from values from $[0,1]$. Voxel-probabilities closer to 0.5 are associated with higher uncertainty.¹⁵ Uncertainty score u_i calculation is described in Equation 1.

$$u_i = -(\text{mean}(|p_i - 0.5|)) \quad (1)$$

Finally, Bayesian models return a probability distribution rather than a single probability. These models can be approximated by generating n predictions from a model that includes a dropout layer.⁵ Images with a wider distributions have higher uncertainty. A dropout layer is added to the last decoding convolutional layer in the 3D U-net model. Performance was compared when dropout was enabled during both training and testing versus only at testing. To localize uncertainty estimation to ROIs, the uncertainty score u_i was calculated by taking the mean of the top 0.1% variances of the probability maps, as shown in Equation 2 where p_{i_j} represents the j th probability map returned by the model for image i .

$$\begin{aligned} \text{var}_i &= \text{var}(p_{i_1}, \dots, p_{i_n}) \\ \text{top}_i &= \text{highest 0.1\% of values in var}_i \\ u_i &= \text{mean}(\text{top}_i) \end{aligned} \quad (2)$$

While uncertainty sampling identifies images unfamiliar to the current model, annotation redundancy restriction prevents annotation of images similar to one another. The first annotation redundancy restriction method selects the most representative uncertain images. Consider a subset of k uncertain, unannotated images. If there are j images, where $j < k$, similar to one another, then annotating only some of j images may be sufficient. To evaluate image similarity, we can compare the high-level features between two images. 3D U-net has both an encoder and decoder arm.¹³ The encoder arm uses multiple convolutional layers in series to generate an array of high-level features. We modified Yang et al.’s approach of using cosine similarity to compare arrays of high level features for 3D images.⁴ The encoder arm returns an 4D array of size $(x, y, z, 512)$, where x, y, z are variable to the size of the input image. The 4D array is then flattened to a 1D array of size 512 by taking the mean across other axes. We can then measure the similarity between two images by calculating the similarity score $ss(I_i, I_j) = \text{cosine_similarity}(h_i, h_j)$ where h_i are flattened high-level features of image i and h_j are that of image j . Next, we use the maximum set cover approach to approximate a subset S_m that most represents the entire set of uncertain, unannotated images S_k (Supplementary Algorithm 1).⁴ S_m begins as an empty set and is iteratively built to maximize the representativeness of S_m for S_k . To quantify how much an image $x \in S_k$ is already represented within S_m , we calculate $f(S_m, x) = \max_{x_i \in S_m} ss(x_i, x)$. Next, we calculate $F(S_m, S_k) = \sum_{x_i \in S_k} f(S_m, x_i)$ to measure how much S_m represents S_k . By iteratively adding the image from S_k that maximizes $F(S_m, S_k)$ until S_m is of size m , we can estimate a subset S_m most representative for S_k .

The second redundancy restriction method selects uncertain images most non-similar to already annotated data. Consider a subset of k uncertain, unannotated images where there are j images, where $j < k$, similar to the images already annotated. Then, annotating images from S_j may not be informative to the model. In order to get a subset $S_m \subset S_k$ that is most non-similar to the set of already annotated images S_a and images already selected to be annotated, we iteratively build S_m by comparing each image in S_k to the images in S_a and those already in S_m , and add the one least similar to these images to S_m from S_k (Supplementary Algorithm 2).

The final investigated AL technique determined the optimal images to initially annotate as opposed to random initialization. We used radiomics feature extraction to build an initial training set with the most diverse features. Radiomic feature extraction was performed with PyRadiomics,

an open-source Python package for extracting radiomic features from medical images.¹⁶ The skull-stripped brain region was used as the mask to focus feature extraction. First-order features, including mean, median, entropy, and energy, were extracted to build a feature array per image. Each feature array was normalized across all feature arrays. An initial dataset was then obtained by iteratively selecting the subset of images that maximizes the minimum Euclidean distance between normalized feature arrays similarly to Supplementary Algorithm 1.

2.3 Experiments

We retrospectively collected T2 and T1ce imaging sequences and clinical data from pediatric patients with intracranial leptomeningeal seeding brain tumors who were admitted to 4 large academic hospitals in Hunan Province, China from January 2011 to December 2018 and to the Children’s Hospital of Philadelphia (CHOP) from January 2005 to December 2019. Exclusion criteria included patients above 18 years old, patients with missing pathological reports or image sequences, or if images were collected after any tumor-reducing treatment. The institutional review boards of all involved institutions approved this study, and the requirement for informed consent was waived.

Manual segmentation of contrast-enhancing tumor was performed by a neuro-oncologist (J.P.) with 7 years of experience, using the Level Tracing and Threshold tools in 3D Slicer (v.4.10). The MR acquisition parameters are shown in Supplementary Figures 1 and 2. 20% of the data was partitioned as the testing set. At each AL iteration, 20% of the annotated training data was used as the validation set. Images were skull stripped, resampled to isotropic resolution, and co-registered to the same anatomical template. For experimentation purposes, all images were proactively annotated for the contrast-enhancing lesion. However, we assign the images unannotated and annotated states based on the images selected by the AL algorithm. Only images with annotated states were used for model training.

Experiment 1 compared different uncertainty sampling techniques. We initialized a random training set of 40 images and trained a preliminary model. We then annotated 50 of the most uncertain, unannotated images (~10% of entire dataset) returned by the uncertainty sampling technique and retrained the model. Model performance was evaluated at each AL iteration.

Experiment 2 compared different annotation redundancy restriction techniques after uncertainty sampling. We initialized a random training set of 40 images and trained a preliminary

model. Of the 100 most uncertain images, we annotated 50 of the most representative images to add to the training data. Because we were interested when the performance of the model is not different to that of the full data model, we use $\alpha = 0.1$ for Experiment 1 and 2.

Experiment 3 compares initial dataset selection using radiomics features of the brain to random initialization. To generate a distribution of model performance trained on random dataset initialization, a model is trained and evaluated on n randomly selected images. This is repeated 10 times. Then, a model is trained on a dataset of size n determined by radiomics and compared in performance to the distribution of random initializations. As we are determining if the methods are statistically different, $\alpha = 0.05$ is used.

3 RESULTS

T2 and T1ce sequences with contrast enhancing tumor segmentation were available for 683 brain MRIs from 683 patients (85 Hunan, 598 CHOP). 39 patients were excluded due to skull stripping failure, and 6 were excluded due to co-registration failure. Characteristics for the remaining 638 patients can be found in Table 1. Each model took approximately 1-5 hours to train depending on the AL iteration or size of the annotated training data. The pre-trained models and the AL framework is publicly accessible at <https://github.com/naddan27/ActiveLearning/>.

Figure 2 compares the mean and median Dice scores of the uncertainty estimation techniques at different percentages of the training data from Experiment 1. Performance of the full data model are taken from its previously published study.¹⁴ Both bootstrapping and Bayesian approximation using dropout at training and testing (dropout traintest) consistently outperformed

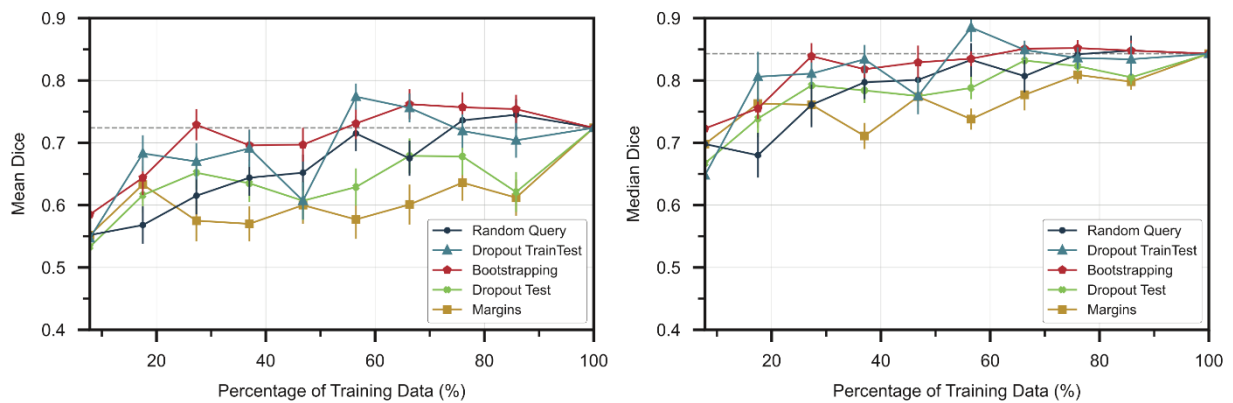


Figure 2. Dice scores of uncertainty techniques at different percentages of training data. Horizontal dashed line is performance with full training data. Error bars represent the standard error.

Table 1. Study Population Characteristics

Characteristics	Number (Percent)
Median age at diagnosis in years: Mean (range)	9.4 (0.1-17.9)
Sex	
Male	355 (55.6%)
Female	283 (44.4%)
Anaplastic astrocytoma	53 (8.4%)
Fibrillary astrocytoma	35 (5.5%)
Glioblastoma	22 (3.4%)
Infiltrating astrocytoma	20 (3.1%)
Pilocytic astrocytoma	119 (18.7%)
Pilomyxoid astrocytoma	13 (2.1%)
Medulloblastoma	72 (11.3%)
Craniopharyngioma	32 (5%)
Dysembryoplastic neuroepithelial tumor (DNET)	25 (3.9%)
Ependymoma	54 (8.5%)
Gangliocytoma/ Ganglioglioma	58 (9.1%)
Meningioma	22 (3.4%)
Neurocytoma	4 (0.6%)
Oligodendroglioma	8 (1.2%)
Pleomorphic xanthoastrocytoma (PXA)	3 (0.4%)
Schwannoma	4 (0.6%)
Subependymal giant cells tumor	10 (1.6%)
Embryonal tumor group	
Atypical teratoid rhabdoid tumor	18 (2.8%)
Pineoblastoma	4 (0.6%)
Primitive neuroectodermal tumor	17 (2.7%)
Germ cell tumor group	
Germinoma	15 (2.4%)
Germ cell tumor	4 (0.6%)
Choroid plexus papilloma	26 (4.1%)

random query. In contrast, margins and Bayesian approximation using dropout only at testing (dropout test) performed worse than random query. For bootstrapping, there was no significant difference in model performance trained with 27.3% ($p = 0.890$) and 27.3% ($p = 0.874$) of the data versus trained with the full data for mean and median Dice, respectively. For dropout traintest, there was no significant difference in model performance trained with 17.5% ($p = 0.293$) and 17.5% ($p = 0.108$) of the data versus trained with the full data for mean and median Dice, respectively.

In Experiment 2 comparing annotation redundancy restriction techniques, dropout traintest was used to identify the uncertain, unannotated images before annotation redundancy restriction due to its performance in Experiment 1 and smaller computational burden than bootstrapping. Table 2 shows the effect of adding an annotation redundancy restriction technique on top of uncertainty sampling versus just uncertainty sampling alone. While both redundancy restriction techniques achieved similar performance to that of the full model before random query, both redundancy restriction techniques were not able to outperform AL strategies that solely used uncertainty sampling. Figure 3 shows examples of predicted segmentations by models that were built using uncertainty and annotation redundancy restriction AL strategies.

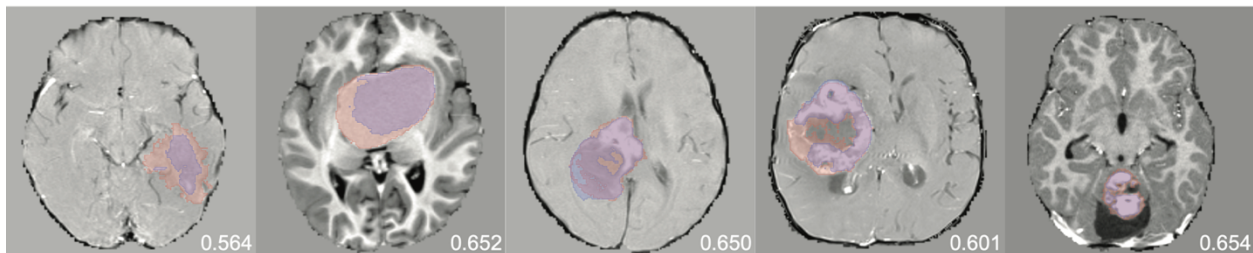


Figure 3. Examples of predicted (blue) vs expert (red) segmentations at 17.5% of training data with random query, dropout traintest, bootstrapping, redundancy representative, and redundancy non-similar in order. Dice scores are shown for each respective image.

In Experiment 3 evaluating for a radiomics based initial dataset selection, radiomics dataset initialization had higher Dice at $n=20$ and 80 than random query, but improvements were not significant. Full comparisons are shown in Table 3.

4 DISCUSSION

We compared multiple uncertainty and representative techniques and evaluated their individual and synergistic performance in reducing the number of annotations needed on real-world, multi-institutional clinical data. We show that an AL framework using Bayesian approximation with dropout at training and testing can achieve state-of-the-art performance with less than 20% of the

Table 2. Mean dice of uncertainty and redundancy reduction methods. First iteration without significant difference to performance of full data model are bolded. Standard deviation in parentheses.

Percentage of Training Data	7.8% n=40	17.5% n=90	27.3% n=140	37.0% n=190	46.8% n=240	56.5% n=290	66.3% n=340	100% n=513
Random Query	0.552 (0.339)	0.568 (0.331)	0.615 (0.335)	0.644 (0.327)	0.652 (0.326)	0.715 (0.307)	0.675 (0.308)	
<i>Uncertainty Only</i>								
Dropout TrainTest	0.547 (0.329)	0.683 (0.321)	0.670 (0.316)	0.691 (0.334)	0.607 (0.345)	0.774 (0.252)	0.756 (0.266)	
Bootstrapping	0.585 (0.331)	0.644 (0.319)	0.729 (0.280)	0.696 (0.296)	0.697 (0.302)	0.731 (0.280)	0.762 (0.265)	0.724 (0.295)
<i>With Dropout TrainTest</i>								
Redundancy Representative	0.547 (0.329)	0.561 (0.332)	0.613 (0.340)	0.663 (0.315)	0.638 (0.315)	0.612 (0.333)	0.707 (0.300)	
Redundancy Non-similar	0.547 (0.329)	0.621 (0.336)	0.590 (0.344)	0.650 (0.329)	0.697 (0.302)	0.651 (0.328)	0.730 (0.284)	
<i>P-values of bolded dice scores: Random Query ($p = 0.814$), Dropout TrainTest ($p = 0.293$), Bootstrapping ($p = 0.890$), Representative ($p = 0.115$), Non-similar ($p = 0.475$)</i>								

Table 3. Brain Radiomics Feature Extraction versus Random Selection for Dataset Initialization

Initial Dataset Size	Random Dice (SD)	Radiomics Dice	p-value
20	0.458 (0.042)	0.526	0.101
40	0.541 (0.030)	0.513	0.349
80	0.535 (0.028)	0.587	0.061

training data. Comparatively, AL with only random query achieved full training data model performance at 56.5% of the training data.

We compared 4 different uncertainty estimation techniques to random query: bootstrapping, margins, dropout traintest, and dropout test. While bootstrapping did reduce training data by 70%, its computational demand can be prohibitive. We were therefore interested in using dropout as an alternative. The primary concern with dropout was that it would not be able to generate distinct enough predictions to generate a reliable uncertainty score.^{2,6} Furthermore, the prediction variability, which is generally concentrated at the ROI, would be diluted by the substantial number of background voxels in 3D imaging. To address this concern, we presented a dropout strategy that focuses on regions of high disagreement within the image to estimate uncertainty. With this strategy, we show that dropout is generalizable to AL in 3D segmentation tasks and in fact superior to bootstrapping. We also attempted removing dropout training stabilization by implementing dropout only at testing to force more diverse predictions. However, model prediction instability had a stronger negative effect in model performance than the possible positive effects of having diverse predictions for uncertainty estimation as demonstrated by the consistently lower than random query performance even with larger percentages of the training data. Results also show that uncertainty estimation may require calibration given the significant amount of noise contributed by the background voxels in 3D imaging. This may explain margins sampling performing worse than random query in our paper despite other studies showing better performance on 2D imaging.²

We were also interested in reducing annotation redundancy. While these techniques were able to achieve similar performance to that of the model trained on the full data with approximately 40%-50% of the training data, they were not able to outperform AL strategies that only incorporate uncertainty. Adding a redundancy restriction strategy can bias training away from uncertain images. Future projects may add a way to prioritize more uncertain images within the representative cohort. Uncertain images can be clustered based on similarity, where each cluster is assigned an overall uncertainty. While only a subset of images from each cluster are selected for annotation, training can be biased toward the uncertain images by artificially increasing images from uncertain clusters with data transformations or generative adversarial networks.¹⁷⁻²¹

Lastly, we evaluate using radiomics features of the brain to construct the initial dataset. At various initial dataset sizes, the performance of the radiomics strategy was not statistically different

from random query, demonstrating that selecting an initial dataset based on high level radiomic features of the brain do not translate to selecting images with diverse tumor characteristics. This is understandable given that radiomic features are very dependent on acquisition parameters and heterogeneity in age groups and histologies. An alternative strategy may be to only consider voxels above a specific intensity within the brain mask to vaguely localize the ROI, though this only applies to tasks that segment contrast-enhancing ROI. This AL strategy may be more applicable for models that accept multiple organ systems or imaging modalities to initialize a dataset balanced in all imaging modalities and organ systems of interest.

The major strength of our study is its demonstration of the specific reduction in annotation burden of each AL technique when applied by itself or when combined with multiple techniques. Recent studies have used combined uncertainty and representative approaches,^{8,10} but as demonstrated in our uncertainty experiments, AL frameworks are sensitive to calibration when applied to real-world, clinical imaging. By doing a detailed analysis of each technique on annotation burden reduction, our study can guide future studies that combine AL techniques. Furthermore, given the calibration sensitivity and need to optimize hyperparameters at each iteration, our study suggests that AL frameworks may benefit from an adaptive strategy as AL iterations are added. Wang et. al incorporates reinforcement learning with Markov models to create an adaptive AL framework for example,¹¹ and our study can be used to understand the adaptive strategies returned by reinforcement learning strategies in future studies.

Our study does have limitations. First, we purposefully used the hyperparameters optimized for the full data model on all AL models to address hyperparameter confounding bias, and therefore, results at each iteration may be lower than if they were trained with hyperparameters optimized for each iteration. We assumed performance would be similarly affected for each iteration. Additionally, we only focus on the top 0.1% of variances for the dropout methods when comparing the uncertainty techniques, while the bootstrapping strategy incorporates all variances, making it more sensitive to background voxel noise. Bootstrapping was tested before the incorporation of focusing on the highest variance voxels, and therefore, bootstrapping was not repeated with this technique given that dropout strategy was able to perform similarly to bootstrapping with a significantly lower computational demand. Furthermore, we randomly split the annotated data into the training and validation set at each AL iteration rather than having a consistent validation set at each iteration. Experiments were designed as such with the thought that

already deployed AL models should continuously look for more informative samples to add to the training data as time passes and more imaging is available. However, this may bias and overfit models to the training data, hindering model performance at larger AL iterations. Lastly, our generalizability of AL techniques onto real-world, clinical data uses a single dataset and single task of brain tumor segmentation. Further studies with different datasets and tasks are needed before AL strategies can be confidently applied onto real-world data.

5 CONCLUSIONS

In conclusion, we assess multiple AL methods and demonstrate their applicability onto real-world clinical 3D brain tumor segmentation. We compare various AL uncertainty estimation as well as annotation redundancy restriction and initial dataset selection strategies, finding that a dropout uncertainty estimation framework is optimal.

FIGURE LEGEND

Figure 1. Workflow of the full active learning framework

Figure 2. Dice scores of uncertainty techniques at different percentages of training data. Horizontal dashed line is performance with full training data. Error bars represent the standard error.

Figure 3. Examples of predicted (blue) vs expert (red) segmentations at 17.5% of training data with random query, dropout traintest, bootstrapping, redundancy representative, and redundancy non-similar in order. Dice scores are shown for each respective image.

ACKNOWLEDGEMENTS

Authors declare no acknowledgements. All participating parties gave significant contributions for project development, data availability, annotation, and interpretation and are listed as authors.

FUNDING

This project was supported by Alpert Medical School Summer Assistantship award to DDK. This work was supported by National Science Foundation of Hunan Province, China (2022JJ30762), International Science and Technology Innovation Joint Base of Machine Vision and Medical Image Processing in Hunan Providence, China (2021CB1013), and the 111 project (B18059) to CZ. This work was supported by Hunan Province Key Areas Research and Development Program, China (2022SK2054) to BZ. This work was supported by Huxiang High-level Talent Gathering

Project-Innovation Talent, China (2021RC5003) to WL. This project was supported by the National Cancer Institute (NCI) of the National Institutes of Health under Award Number R03CA235202 to HXB. This work was supported by the Natural Science Foundation of China (81971696 to LY), Natural Science Foundation of Hunan Province (2022JJ30861 to LY), and Sheng Hua Yu Ying Project of Central South University to LY.

CONFLICTS OF INTEREST

Authors declare no conflict of interest.

DATA AVAILABILITY

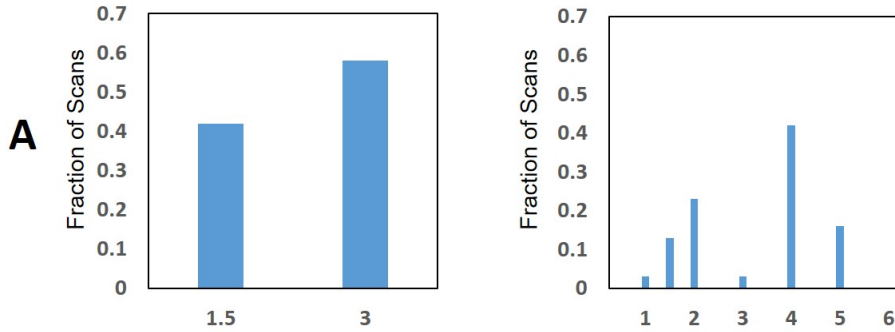
Data used is not publicly available for patient confidentiality. Interested parties may contact authors regarding questions on data.

6 REFERENCES

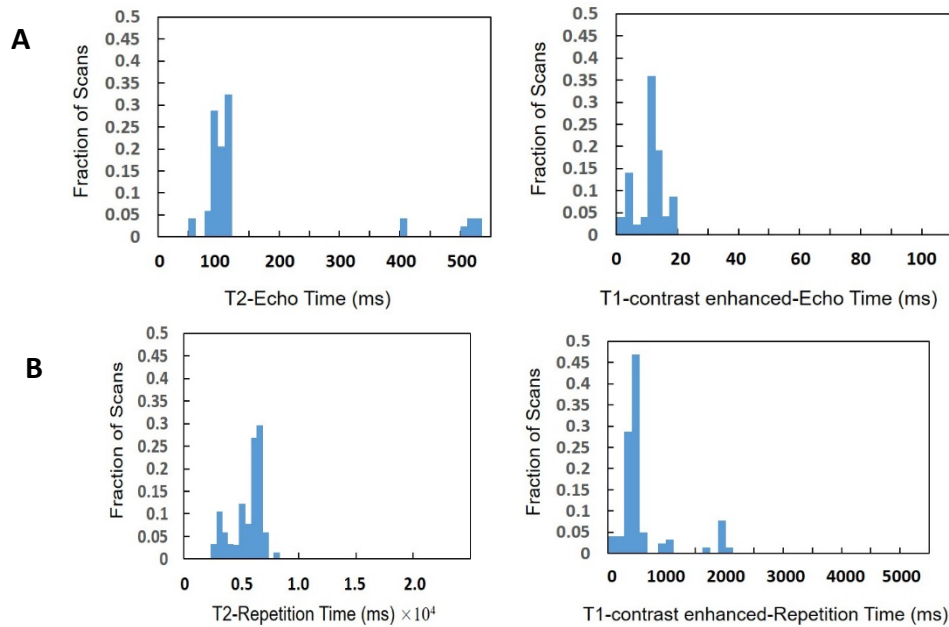
1. Bakas S, Reyes M, Jakab A, et al. Identifying the Best Machine Learning Algorithms for Brain Tumor Segmentation, Progression Assessment, and Overall Survival Prediction in the BRATS Challenge. 2018:arXiv:1811.02629. Accessed November 01, 2018. <https://ui.adsabs.harvard.edu/abs/2018arXiv181102629B>
2. Budd S, Robinson EC, Kainz B. A survey on active learning and human-in-the-loop deep learning for medical image analysis. *Med Image Anal.* Jul 2021;71:102062. doi:10.1016/j.media.2021.102062
3. Wang K, Zhang D, Li Y, Zhang R, Lin L. Cost-Effective Active Learning for Deep Image Classification. 2017:arXiv:1701.03551. Accessed January 01, 2017. <https://ui.adsabs.harvard.edu/abs/2017arXiv170103551W>
4. Yang L, Zhang Y, Chen J, Zhang S, Chen DZ. Suggestive Annotation: A Deep Active Learning Framework for Biomedical Image Segmentation. 2017:arXiv:1706.04737. Accessed June 01, 2017. <https://ui.adsabs.harvard.edu/abs/2017arXiv170604737Y>
5. Gal Y, Ghahramani Z. Dropout as a Bayesian Approximation: Representing Model Uncertainty in Deep Learning. 2015:arXiv:1506.02142. Accessed June 01, 2015. <https://ui.adsabs.harvard.edu/abs/2015arXiv150602142G>
6. Gal Y, Islam R, Ghahramani Z. Deep Bayesian Active Learning with Image Data. 2017:arXiv:1703.02910. Accessed March 01, 2017. <https://ui.adsabs.harvard.edu/abs/2017arXiv170302910G>
7. Smailagic A, Noh HY, Costa P, et al. MedAL: Deep Active Learning Sampling Method for Medical Image Analysis. 2018:arXiv:1809.09287. Accessed September 01, 2018. <https://ui.adsabs.harvard.edu/abs/2018arXiv180909287S>
8. Kim ST, Mushtaq F, Navab N. Confident Coreset for Active Learning in Medical Image Analysis. *arXiv preprint arXiv:200402200*. 2020;
9. Warren KE, Vezina G, Poussaint TY, et al. Response assessment in medulloblastoma and leptomeningeal seeding tumors: recommendations from the Response Assessment in Pediatric Neuro-Oncology committee. *Neuro Oncol.* Jan 10 2018;20(1):13-23. doi:10.1093/neuonc/nox087
10. Sharma D, Shanis Z, Reddy CK, Gerber S, Enquobahrie A. Active Learning Technique for Multimodal Brain Tumor Segmentation Using Limited Labeled Images. Springer International Publishing; 2019:148-156.
11. Wang J, Yan Y, Zhang Y, Cao G, Yang M, Ng MK. Deep Reinforcement Active Learning for Medical Image Classification. Springer International Publishing; 2020:33-42.
12. Li H, Yin Z. Attention, Suggestion and Annotation: A Deep Active Learning Framework for Biomedical Image Segmentation. Springer International Publishing; 2020:3-13.
13. Ronneberger O, Fischer P, Brox T. U-Net: Convolutional Networks for Biomedical Image Segmentation. 2015:arXiv:1505.04597. Accessed May 01, 2015. <https://ui.adsabs.harvard.edu/abs/2015arXiv150504597R>

14. Peng J, Kim DD, Patel JB, et al. Deep Learning-Based Automatic Tumor Burden Assessment of Pediatric High-Grade Gliomas, Medulloblastomas, and Other Leptomeningeal Seeding Tumors. *Neuro Oncol.* Jun 26 2021;doi:10.1093/neuonc/noab151
15. Settles B. Active learning literature survey. 2009;
16. van Griethuysen JJM, Fedorov A, Parmar C, et al. Computational Radiomics System to Decode the Radiographic Phenotype. *Cancer Res.* Nov 1 2017;77(21):e104-e107. doi:10.1158/0008-5472.Can-17-0339
17. Li Y, Chen J, Xie X, Ma K, Zheng Y. Self-Loop Uncertainty: A Novel Pseudo-Label for Semi-Supervised Medical Image Segmentation. 2020:arXiv:2007.09854. Accessed July 01, 2020. <https://ui.adsabs.harvard.edu/abs/2020arXiv200709854L>
18. Last F, Klein T, Ravanbakhsh M, Nabi M, Batmanghelich K, Tresp V. Human-Machine Collaboration for Medical Image Segmentation. *ICASSP 2020 - 2020 IEEE International Conference on Acoustics, Speech and Signal Processing (ICASSP)*. 2020:1040-1044.
19. Venturini L, Papageorghiou AT, Noble JA, Namburete AIL. Uncertainty Estimates as Data Selection Criteria to Boost Omni-Supervised Learning. presented at: Medical Image Computing and Computer Assisted Intervention – MICCAI 2020: 23rd International Conference, Lima, Peru, October 4–8, 2020, Proceedings, Part I; 2020; Lima, Peru. https://doi.org/10.1007/978-3-030-59710-8_67
20. Mahapatra D, Bozorgtabar B, Thiran J-P, Reyes M. Efficient Active Learning for Image Classification and Segmentation Using a Sample Selection and Conditional Generative Adversarial Network. Springer International Publishing; 2018:580-588.
21. Wang H, Rivenson Y, Jin Y, et al. Deep learning enables cross-modality super-resolution in fluorescence microscopy. *Nature Methods.* 2019/01/01 2019;16(1):103-110. doi:10.1038/s41592-018-0239-0

Supplementary Figure 1. Magnetic field strength and slice thickness of (A) CHOP for T2 and T1-contrast enhanced images



Supplementary Figure 2. (A) Echo time for T2 and T1-contrast enhanced MRI images of CHOP; (B) Repetition time for T2 and T1-contrast enhanced MRI images of CHOP



Supplemental Algorithm 1 Representative subset within uncertain, unannotated images

-
- 1: Initialize $S_m \leftarrow \{\}$
 - 2: Initialize $S_k \leftarrow$ set of k unannotated images with highest uncertainty
 - 3: Move random image from S_k to S_m
 - 4: **while** $size(S_m) < m$ **do**
 - 5: **Set** $F_{max} \leftarrow 0, x_{max} \leftarrow none$
 - 6: **for all** images $x_i \in S_k$ **do**
 - 7: Temporarily move x_i from S_k to S_m

```

8:         Calculate  $F(S_m, S_k)$ 
9:         if  $F(S_m, S_k) > F_{max}$  then
10:              $F_{max} \leftarrow F(S_m, S_k)$ 
11:              $x_{max} \leftarrow x_i$ 
12:         end if
13:         Move  $x_i$  back from  $S_m$  to  $S_k$ 
14:     end for
15:     Move  $x_{max}$  from  $S_k$  to  $S_m$ 
16: end while

```

Supplemental Algorithm 2 Subset of uncertain unannotated images non-similar to already annotated images

```

1: Initialize  $S_m \leftarrow \{\}$ 
2: Initialize  $S_k \leftarrow$  set of  $k$  unannotated images with highest uncertainty
3: Move random image from  $S_k$  to  $S_m$ 
4: while  $size(S_m) < m$  do
5:     Set  $ss\_sum_{min} \leftarrow +\infty$ ,  $x_{min} \leftarrow none$ 
6:     for all images  $x_i \in S_k$  do
7:          $similarity\_sum \leftarrow 0$ 
8:         for all images  $x_j \in (S_a \cup S_m)$  do
9:              $similarity\_sum += ss(x_i, x_j)$ 
10:        end for
11:        if  $similarity\_sum < ss\_sum_{min}$  then
12:             $ss\_sum_{min} \leftarrow similarity\_sum$ 
13:             $x_{min} \leftarrow x_i$ 
14:        end if
15:    end for
16:    Move  $x_{min}$  from  $S_k$  to  $S_m$ 
17: end while

```